Electrical, Thermal and Optical Diagnostics of an Atmospheric Plasma Jet System

Nwankire, C. E., Law, V. J., Nindrayog, A., Twomey, B., Niemi, K., Milosavljević, V., Graham, W. G., & Dowling, D. P. (2010). Electrical, Thermal and Optical Diagnostics of an Atmospheric Plasma Jet System. *Plasma Chemistry and Plasma Processing*, *30*(5), 537-552. https://doi.org/10.1007/s11090-010-9236-5

Published in:
Plasma Chemistry and Plasma Processing

Plasma Chem Plasma Process
DOI 10.1007/s11090-010-9236-5

ORIGINAL PAPER

Electrical, Thermal and Optical Diagnostics of an Atmospheric Plasma Jet System

C. E. Nwankire · V. J. Law · A. Nindrayog · B. Twomey · K. Niemi · V. Milosavljević · W. G. Graham · D. P. Dowling

Received: 22 February 2010 / Accepted: 28 May 2010

Abstract Plasma diagnostics of atmospheric plasmas is a key tool in helping to understand processing performance issues. This paper presents an electrical, optical and thermographic imaging study of the PlasmaStream atmospheric plasma jet system. The system was found to exhibit three operating modes; one constricted/localized plasma and two extended volume plasmas. At low power and helium flows the plasma is localized at the electrodes and has the electrical properties of a corona/filamentary discharge with electrical chaotic temporal structure. With increasing discharge power and helium flow the plasma expands into the volume of the tube, becoming regular and homogeneous in appearance. Emission spectra show evidence of atomic oxygen, nitric oxide and the hydroxyl radical production. Plasma activated gas temperature deduced from the rotational temperature of nitrogen molecules was found to be of order of 400 K: whereas thermographic imaging of the quartz tube yielded surface temperatures between 319 and 347 K.

Keywords Plasma jet · Diagnostics · Plasma diagnostics · Optical emission · Infrared thermography · Corona

C. E. Nwankire (✉) · B. Twomey · D. P. Dowling (✉)
School of Mechanical and Materials Engineering, University College Dublin, Belfield, Dublin 4, Ireland
e-mail: charles.nwankire@ucd.ie

D. P. Dowling
e-mail: denis.dowling@ucd.ie

V. J. Law · V. Milosavljević
National Centre for Plasma Science and Technology, Dublin City University, Glasnevin, Dublin 9, Ireland

A. Nindrayog · K. Niemi · W. G. Graham
Centre for Plasma Physics, Department of Physics and Astronomy, Queen's University Belfast, Belfast BT7 1NN, Northern Ireland

V. Milosavljević
Faculty of Physics, University of Belgrade, Belgrade, Serbia

Published online: 27 June 2010

Introduction

Since first reported in 1968 [1], low temperature atmospheric pressure plasmas (APP) have been deployed for many material processing applications [2, 3]. One of the most widely used APP applicators is the tube design which includes: the plasma jet [4, 5], plasma needle [6], plasma pencil [7], and microplasma jet [8]. The plasma operational modes of these tube sources are influenced by their electrode configuration, gas flow rate, gas type, applied power and the distance between the plasma applicator nozzle and treated surface [9–11]. This study is focused on the examination of an industrial scale low temperature atmospheric plasma jet system called PlasmaStream^{TM} [12, 13]. The main difference between this system and the plasma needle, pencil and microplasma jet systems is the electrode structure, the increased electrode to treated surface distance and the increased nozzle area. Amongst the applications reported to-date of this source are: enhancing silicone adhesion to steel [14, 15], control of cell adhesion [16] and the deposition of plasma polymerized coatings [17, 18]. From these studies it has been concluded that parameters such as applied power and the gap distance between the substrate and the jet nozzle significantly influence deposited coating properties. For example for the deposition of plasma deposited primer coatings prior to bonding of siloxane elastomers to stainless steel, increasing the gap distance resulted in primer coatings exhibiting significantly reduced adhesive bond strengths [19]. Understanding the nature of the initiating plasma, the thermal properties of the system and the effect on these properties of the operating parameters i.e., input power, gas flow and the effect of the source to substrate distance is a critical first step towards determining the plasma kinetics and thus potential range of applications of atmospheric plasma jets. This paper investigates these issues through a systematic study of the electrical, optical emission and thermal properties of this plasma jet system.

Experimental Methods

Atmospheric Pressure Plasma Jet

The diagnostic study was carried out on the PlasmaStream^{TM} atmospheric pressure plasma jet (APPJ) system developed by Dow Corning. This system is driven by a Plasma Technics Inc [20] high voltage power source operating in the 10–25 kHz range. This high voltage source uses a flyback transformer which produces a non sinusoidal voltage waveform due to the rapid collapse of the magnetic circuit within the flyback transformer [21]. Further to this, the APPJ differs from cross-field and linear-field tube [22] devices, as the high voltage power source is directly connected to two parallel tungsten needle electrodes mounted in Techtron® housing, and spaced 12 mm apart. This arrangement is positioned at one end of a tube, which typically is made of a 19 mm outside diameter quartz tube (16 mm inside diameter) and a length of 72 mm (these values equate to an internal volume of 14.47 cm^{-3}). A detailed experimental study resulting in a two-dimensional model during the operation of a single electrode needle-plane geometry under pre-vacuum pumped conditions can be found in reference [23]. In this the reactor the needle tip-dielectric gap distance is 3 mm and the operating peak to-peak voltage is 2.8 kV. In contrast the plasma jet system under examination here has two needles with a minimum needle tip-dielectric gap distance of 10 mm, with an estimated total exposed area of 0.5 cm^2, and the operating peak-to-peak voltage of the order of 16 kV. A schematic diagram of the device and its

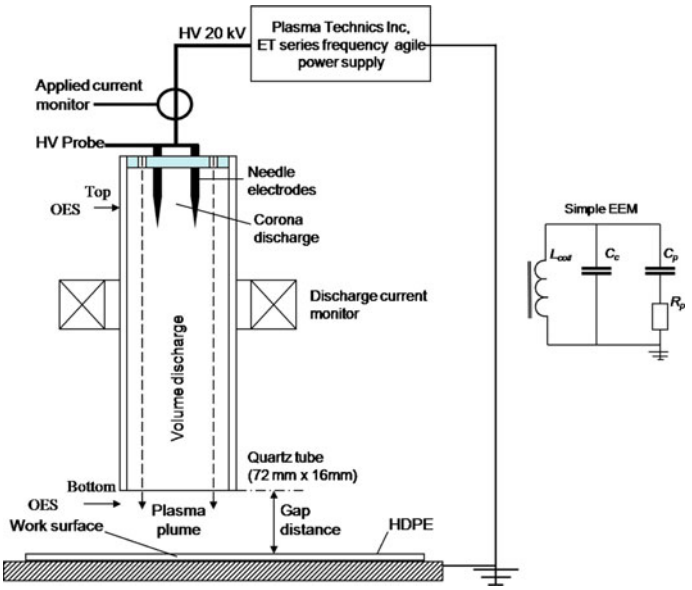

Fig. 1 A schematic diagram of the APPJ system showing the two positions of the current monitor, voltage probe, optical spectrometer and electrode configuration and electrical equivalent model

equivalent electrical model (EEM) is shown in Fig. 1. The working gas is injected between the needle electrodes and flows out through the quartz tube nozzle. A corona plasma discharge is produced whose visual morphology varies with gas flow [14, 18]. The helium flow rate of 1–10 standard litres per minute (slm) is controlled using manual valved rotameters. The plasma applicator is mounted onto a XYZ table which allows the plasma jet to target a 2-dimensional or 3-dimensional process parts. The helium plasma extends out of the nozzle to produce a plasma plume, which is directed onto the substrate. The latter is placed on a 10 mm thick sheet of high density polyethylene (HDPE) mounted on an aluminium substrate table. The distance from the nozzle of the quartz tube and the substrate holder is known as the gap distance. The developed power within the discharge jet was set using the controls of the power supply. Here a dial reading 0–100 sets the power delivered to the circuit; and this is referred to as the 'set power'. Finally the surface temperature of the quartz tube was monitored using an InfraTec VarioCAM® high resolution infrared thermographic camera in a similar procedure as reported in reference [24].

Electrical Measurements

In previous studies the plasma jet electrical parameters have been reported as either a percentage of power [18], or simply as a fixed voltage [25]. As the initial breakdown produces a corona discharge and then proceeds to a uniform volume discharge at higher powers and higher helium flow rate, understanding the electrical and gas flow dynamics is critical to assist in the control of the plasma deposition process [14–18, 24, 25]. In this study the applied voltage was measured using a North Star PVM-5 high voltage probe with a ratio of (1 V per kV), which was directly connected to the electrodes. The current measurements were obtained with a Bergoz Instrumentation France, toroidal current transformer (CT–E5.0) with an output of 5 V per Ampere. The current and voltage

waveforms were monitored using National Instruments 2 channel digitizer (−3 dB 100 MHz bandwidth) and LabVIEW 8.2 software. The drive frequency was determined from the voltage waveform as the output exhibited the least distortion and gave the highest signal-to-noise-ratio. As both current and voltage waveforms are highly distorted the use of peak and average values are inappropriate to characterize the discharge. In this paper we use the RMS of the voltage and current waveforms over a time period of approximately 0.1 s using LabVIEW 8.2 software. This procedure yields an estimation of the average DC power, namely ($P = IV$) of the non-sinusoidal waveforms, see (1).

$$(V_{rms} x I_{rms}) = P_{average}(W) \tag{1}$$

Current was measured at two different points to derive the applied power in the drive circuit and the discharge power in the plasma region. This was performed by placing the current monitor at the high voltage lead of the flyback transformer and around the plasma tube, respectively. See Fig. 1.

Optical Emission Spectroscopy

The optical emission from the discharge was monitored using two Ocean Optics spectrometers. The HR4000 covers the 295–395 nm spectral region with a resolution of 0.12 nm full width at half maximum (FWHM), while the USB4000 UV/VIS spectrometer covers the 200–850 nm region, with a resolution of 1.2 nm FWHM. A qualitative overview of the plasma chemistry is obtained from the 200–850 nm data by analyzing the observed line and band emission intensities resulting from different excitation and ionization processes in the plasma. The 295–395 nm data was used to determine rotational temperatures from the band emission of the second positive system of molecular nitrogen $N_2\left(C^3\Pi^+{}_u - B^3\Pi^+{}_g\right)$.

Results and Discussion

In this study the influence of operating the APPJ under typical processing conditions on the electrical, optical emission and thermal properties of the plasma jet is evaluated. The range of processing conditions investigated is given in Table 1. The discussion of the results is presented in two sections. The first considers the electrical characterisation of the jet system, while the second section deals with emission spectroscopy and thermal measurements.

Electrical Characterization

Characterization of Discharge Power as a Function of Set Power

The results of the initial electrical power characterization of the APPJ performed at a gap distance of 2.5 mm and a helium gas flow of 5 slm as a function of set power is shown in

Table 1 Range of plasma jet processing conditions investigated

Set power (a.u.)	He flow rate (slm)	Gap distance (mm)
5–100	1–10	2.5, 5 and 7.5

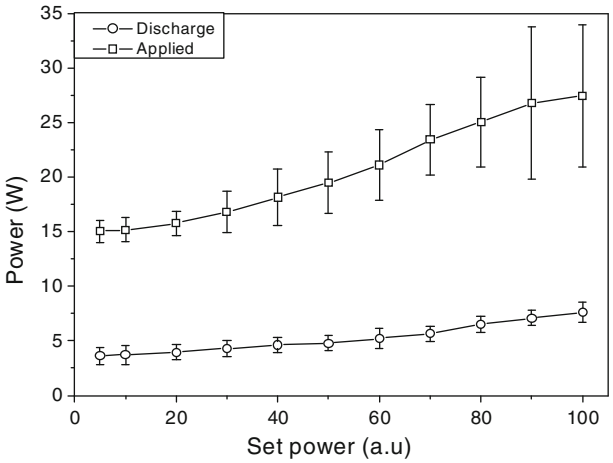

Fig. 2 Calculated discharge and applied power as a function of set power. The *error bars* are the standard deviations over at least 10 runs

Fig. 2. The results demonstrate that the applied plasma power increases linearly from 15 to 27 W; and the discharge plasma power from 4 to 8 W, within the set power range. This is in agreement with the recent results of Herbert et al. [24] for a similar APP jet system. Although there is a degree of uncertainty in the rf ground return path using this method, the measurements demonstrate the importance of measuring discharge power at the plasma rather than using the applied power measured at the input circuit.

The relationships between discharge power and I_{rms} and V_{rms} are shown in Fig. 3a, where it can be seen that the I_{rms} steadily increases at a rate 0.33 mA/W; while the variation of V_{rms} indicates three operating regimes, which correspond to changes in the visual morphology of the plasma. In the first, low power, regime, from 2.2 to 4.7 W, V_{rms} increases at a rate of 0.8 kV/W, the visible plasma is seen to be constricted This regime, could be regarded as corona discharge or constricted glow [26]. In the second regime, from 4.7 to 6.5 W; the visual plasma is expanding into the volume, and V_{rms} is independent of power before increasing again at the rate 0.5 kV/W. This I–V behaviour is associated with a normal glow and subsequent transition to abnormal glow respectively. Analysis of the discharge impedance, Z_p ($Z_p = V_{rms}^2/P$), at the inflection points of the (I–V) curve, indicates that Z_p is at a maximum at the low discharge power, progressively diminishes in the corona discharge regime as the power increases and as the plasma expands into the volume in the normal glow regime, and then is almost constant, with perhaps a slight decrease in the abnormal regime (Fig. 3a).

Figure 3b shows the resonant drive frequency of the system as a function of discharge power at a gap distance 2.5 mm and 5 slm helium flow rate. It should be noted that the resonant drive frequency exhibits an inverse relationship to the discharge power. At 3.6 W discharge power the drive frequency is 18.3 kHz, and falls to 16.8 kHz at 7.6 W. The straight line is a fit to an equivalent electrical model calculated using (2). The shift in resonant drive frequency (f_O) can be explained by frequency pulling on the flyback power supply [27, 28]. Here the frequency pulling as stated in (2) is used as a measure of the frequency change due to a non-ideal load. In the case of the plasma jet system it has a reactive component: output of Flyback transformer (inductive) and chamber and plasma

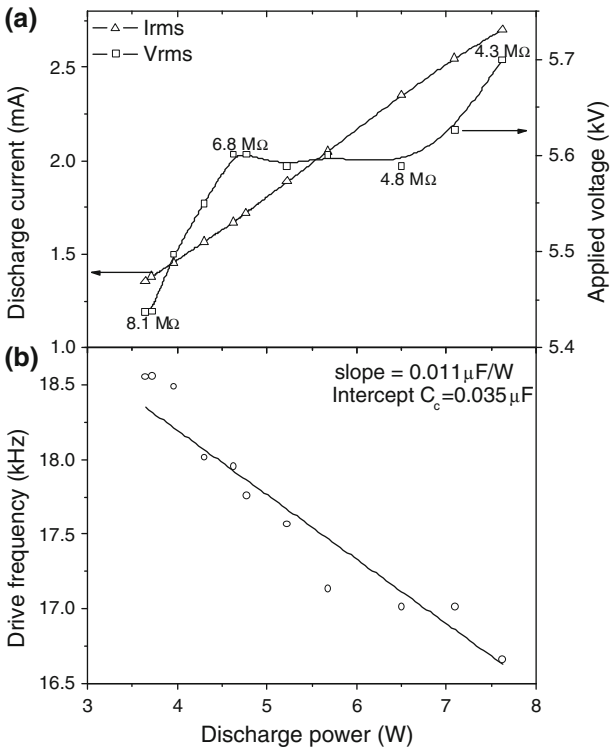

Fig. 3 The dependence of **a** the discharge current, applied voltage and discharge impedance and **b** drive frequency on the discharge power

are capacitive ($C_c + C_p$), and in parallel [28]. This equation is a simple equivalent electrical model (EEM) of the plasma coupled directly through the chamber to the oscillator of the drive circuit power supply, and is used to understand the frequency dynamics of the discharge.

$$f_O = \frac{1}{2\pi\sqrt{L_{coil}(C_c + C_p)}} \tag{2}$$

Using the knowledge of the turns ratio of the secondary coil, an estimated value of between 2 and 10 mH was determined for L_{coil}. The pulling of the resonant drive frequency is modelled using, C_c and C_p as fitting variables. The curve for $L_{coil} = 2$ mH from this EEM is shown in Fig. 3b. Linear extrapolation to the y-axis (0 W) yields a chamber capacitance (0.035 μF) and the slope show that the discharge capacitance is increasing at a rate of 0.011 μF/W, from which the plasma capacitance at any given discharge power can be calculated.

Given that the tube has a fixed volume of 14.47 cm^{-3}, the EEM simulation is consistent with the observation that the system impedance is falling with discharge power as the discharge fills the quartz tube. Under increasing discharge power or increasing helium flow rate the discharge expands to the HDPE layer creating an additional capacitance to ground. For sake of simplicity we included this additional term in C_p. It is further noted that as the plasma expands C_p is expected to increase at a proportional rate. This aspect of the discharge dynamics is explored further in below the section.

Characterization of Discharge Power as a Function of Helium Flow

Figure 4 shows the discharge power, current and applied voltage as dependence on helium flow (1–10 slm) at 50 a.u. set power, which equates to 0.9–5.2 W discharge power for the three gap distances,: 2.5, 5, and 7.5 mm. The results show that the discharge power and current increase with helium flow, whereas the applied voltage decreases. They also show that the discharge power and current increase as the gap distance decreases, with the reverse being true for the applied voltage It is expected that as the helium flow rate increases, the ionization and conductivity of the plasma will also increase: this will subsequently increase the amount of discharge per unit volume and thus the maximum current and discharge power [29]. The decreasing voltage as the helium flow rate increased may be due to a reduction in back diffuse effect of air [10, 30] and thus the quenching effect of oxygen. While the observed increase in the discharge current and power as the gap distance decreases is likely to be due to the enhanced ground electrical return, through the work

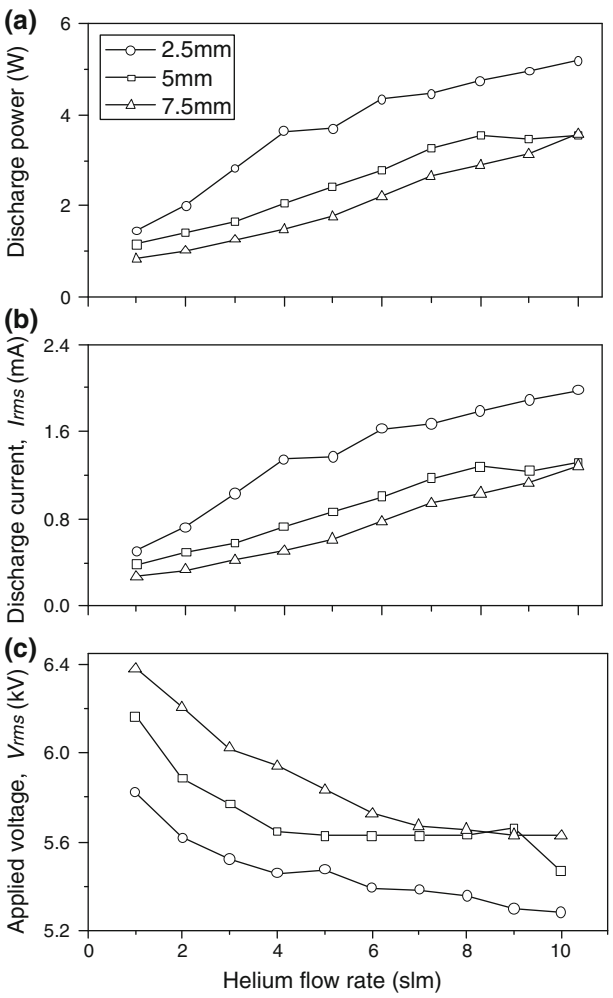

Fig. 4 Discharge power (**a**), discharge current I_{rms} (**b**) and applied voltage V_{rms} (**c**) as a function of helium flow rate and gap distance

surface. The drive frequency was found to increase from 11 to 18 kHz as the gap distance increased from 2.5 to 7.5 mm.

The discharge current, *I*, and applied voltage *V* phase-space diagram over 3 drive frequency periods, for 1, 4, and 10 slm helium flow rates, at a constant gap distance of 2.5 mm are shown in Fig. 5a–c. The voltage in these phase-space diagrams is a convolution of the gap voltage between the needles and the dielectric. This is determined by the charge on the dielectric surface and voltage developed by the collapse of the Flyback transformer magnetic field. The feature in the upper left quadrant of Fig. 5a reflects the corona/filamentary behaviour of the discharge and the feature in the bottom right quadrant are a feature of the flyback transformer.

At a helium flow rate of 1 slm case (Fig. 5a), the I–V phase-space diagram exhibits a chaotic attractor [31]. In the bottom right quadrant the attractor comprises three positive current spikes overlaying each other at the maximum negative voltage point. This is due to the collapse of the magnetic field within the flyback transformer and the releases of the stored energy held within the magnetic gap. In the top left quadrant the attractor has three sets of two negative spikes of different amplitudes and time delays. The six current spikes are approximately 1 micro-second in width and fall within a 15 μs envelope. These current spikes are due to the discharge having irregular temporal and spatial electrical properties. Under this chaotic condition the discharge impedance is 23 MΩ and drive frequency is 18 kHz. With increasing helium flow (Fig. 5b, c) the phase-space attractor becomes periodic, or cyclic, where a single discharge negative current spike of approximately 15 μs per period. The time delay of these current spikes is similar to that of the current envelope produced at low flow rate (Fig. 5a). The discharge impedance and the drive frequency also decrease with helium flow: 11 MΩ at 14 kHz for 6 slm helium flow and 5 MΩ at 11 kHz

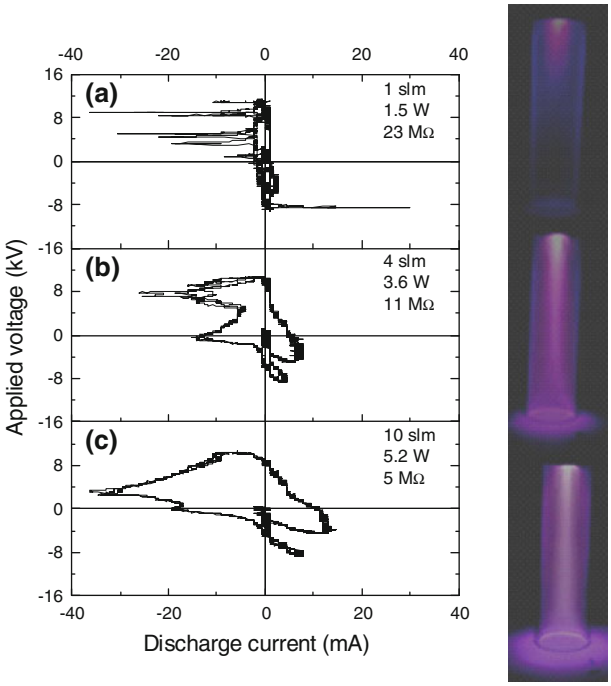

Fig. 5 Discharge current-applied voltage phase-space diagrams and their dependence on helium flow rate. To the right of each phase-space diagram is the associated discharge time average digital image

for 10 slm of helium flow. A computed peak current density for these conditions provides values from of 10 to 70 mA/cm^2.

The associated time averaged digital image of each discharge is shown to the right of each phase space diagram in Fig. 5. These time averaged images illustrate that the discharge is constricted around the electrodes at 1 slm, and then progressively expands in the chamber as the helium flow is increased. This change in current waveform morphology is accompanied by an expansion of the discharge into the chamber volume and illustrated in the associated time average digital images.

The time average digital images in Fig. 5 are taken from a series of 1–10 slm images of the discharge at a gap distance of 2.5 mm. Using National Instruments LabVIEW Vision builder AI 3.5 software a local threshold algorithm obtained an estimation of tube filling rate for helium flows in the 1–3 and 4–10 slm range, which are typical of the constricted corona/filamentary mode and expansion mode, respectively. These calculations yield 1.88 ± 0.15 cm^3/slm for the constricted corona mode and 1.97 ± 0.25 cm^3/slm for the expansion mode.

For helium flow rates of 1–10 slm, the residence time τ of the gas was computed as follows: $\tau = V_{ol}/Q_T$; where V_{ol} is the quartz tube volume [litres], and Q_T is the gas flow rate [litres/min]). With increase in helium flow rate its residence time decreased from 14.5 to 1.4 ms. The helium gas velocity v, ($v = Q_V/A$; where Q_V is the volumetric flow rate [ms^{-3}], and A is the cross-sectional area [m^2]) linearly increased from 0.1 to 0.8 ms^{-1}, for helium flow rate 1–10 slm (see Fig. 6). At low gas velocity, the helium residence time is high and as detailed earlier the plasma is constricted around the electrodes; however, as the gas velocity increases, the residence time decreases, as the plasma expands into the volume.

The homogeneity of ion and radical densities, as well as the dispersion of the precursor in the plasma is reported to depend strongly on the flow conditions in the plasma chamber [32]. These flow conditions are described by the Reynolds number (Re), which is generally used to determine if the flow is laminar or turbulent. Laminar flow is driven by high momentum diffusion and low momentum convection [32]. Equation (3) describes these conditions, where Q_V is the volumetric flow rate [ms^{-3}], L is the length of the quartz tube [m], A is the cross sectional area of the quartz tube [m^2], υ ($\upsilon = \mu/\rho$) is the gas kinematic viscosity (a measure of the gas resistive flow in the tube under the influence of gravity) [ms^{-2}]; μ is the dynamic viscosity (a measure of the gas resistance to flow;

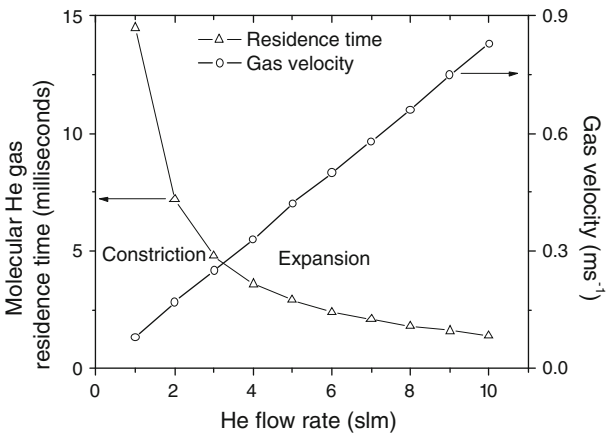

Fig. 6 Molecular helium residence and gas velocity as a function of helium flow rate

2×10^{-5} kg ms^{-1} for helium gas), and ρ is the density (0.166 kg m^{-3} for helium gas at 1 atmosphere, 300 K). The volume of the discharge tube was calculated as 1.4×10^{-5} m^3 (0.014 l). For these conditions the Re varies from 11 to 106. This is well within the laminar flow regime in view of the fact that the transition to the turbulent regime usually occurs at Re > 1,700–2,300 [21].

$$\mathrm{Re} = \frac{Q_V L}{vA} \tag{3}$$

Optical Emission Spectroscopy and Thermal Measurements

Optical Emission Spectroscopy

Figure 7 shows OES spectra taken at the (top) electrode region and the (bottom) nozzle exit for 2.5 mm gap distance, at a discharge power of 7.6 W, and 5 slm helium flow. The emission of the second positive system of molecular nitrogen $N_2\left(C^3\Pi^+{}_u - B^3\Pi^+{}_g\right)$ dominates. The corresponding vibrational band heads, $v = 0 \rightarrow 0, 1, 2, 3$ are located at the wavelengths, $\lambda = 337, 358, 380$, and 406 nm, respectively. At $\lambda = 391$ nm the $v = 0 \rightarrow 0$ band of the first negative system of molecular nitrogen ions $N^+{}_2\left(B^2\Sigma^+{}_u - X^2\Sigma^+{}_g\right)$ is observed.

From an applications perspective the observation of lines from atomic oxygen, nitric oxide and the hydroxyl radicals are particularly significant. Triplet lines from atomic species are found in the near-infrared region: He($3d^3D$–$3p^3P$) at 589 nm, He($3p^3P$–$3s^3S$) at 706 nm and O($3p^5P$–$3s^5S$) at 777 nm. While in the UV emission band, OH radicals

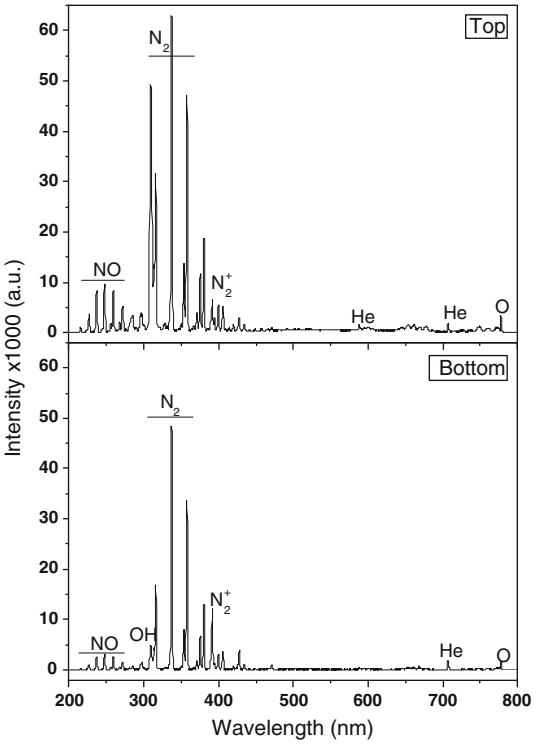

Fig. 7 Optical emission spectra from the APPJ taken from the *top* (electrode region) and *bottom* (nozzle) with a gap distance of 2.5 mm, discharge power of 7.6 W, and helium gas flow of 5 slm

$OH(A^2\Sigma^+ - X^2\Pi)$ around 309 nm are found as well as the γ-bands of nitrogen oxide $NO(A^2\Sigma_u - X^2\Pi)$ below 300 nm.

The observed emission lines from the non-helium species (Fig. 7) are likely to indicate back diffusion of humid air into the atmospheric plasma discharge system; although other potential sources of these species are impurities in the helium supply or some etching of the quartz tube. The OH emission might be expected as a result of dissociation of water molecules, present as moisture in air. Emission from the $N_2^+\left(B^2\Sigma^+{}_u\right)$ state is the dominant emission from the ionized species because the excited $N_2^+\left(B^2\Sigma^+{}_u\right)$ state is populated in most resonant Penning ionization of nitrogen ground state molecules by helium metastables and dimers [33].

The excited atomic species are formed in different ways. Helium (He (3^3S)) is mainly produced by electron-impact excitation of He(2^3S) metastables, which has an electron energy threshold (E_T) value of 2.9 eV, and dissociative recombination of He_2^+ with low-energy electrons rather than by direct electron-impact excitation of ground state He ($E_T = 22.7$ eV) [34]. Atomic oxygen (O ($3p^5P$)) atoms can be produced by electron-impact excitation from ground state O atoms ($E_T = 10.7$ eV) or via quenching reactions involving NO or OH radicals. The H-Balmer-α line at $\lambda = 656$ nm, indicating excited H ($n = 3$) atoms, is not observed, since both the threshold energy ($E_T = 12.1$ eV) is higher, and the degree of moisture in the back diffusing air is small compared to the oxygen content. It is, however, unclear, why no emission lines of atomic nitrogen are observed, e.g., the N ($3p^4S^0$–$3s^4P$) triplet line at $\lambda = 744$ nm with a threshold energy of 12.0 eV, since N and O ground state atoms are assumed to be present in roughly comparable concentrations.

Great care must be taken in interpreting the physical and chemical environment of the plasma from temporally and spatially integrated spectra for several reasons: Firstly the plasma has distinct spatial structures, for example the highly energetic electrons required to directly ionize helium atoms with threshold energies (E_T) = 19.8 eV, or populate helium metastable states, ($E_T = 24.6$ eV), or directly ionize ground state N_2 ($E_T = 15.6$ eV) are only found near the electrodes, since electron mean free paths are short. Secondly this is essentially a pulsed discharge with electron collisions important during the discharge phase, while heavy particle collisions, particularly involving metastable states of both helium and nitrogen [33, 35] dominate in the afterglow of the discharge.

Within these constraints, however, it can be useful to study the relative changes in the intensity of the emission lines such as those shown in Fig. 8. In this figure the ratios are calculated using the intensity of the N_2 line at 337 nm as the denominator. The main excitation process for the upper C $^3\Pi$ state is via electron impact excitation with E_T of about 11 eV. The most pronounced feature in Fig. 8 is the change in all the ratios when the power increases above 4.5 W. This corresponds to the transitions observed visually and in the electrical data, confirming a change in the plasma properties at this point. The trend is for the ratios to increase. Given the relative electron impact excitation threshold energies, it would be tempting to suggest that this was due to an increase in the electron temperature. However, the influence of heavy particles must also be taken into account as detailed previously [33, 35].

Infrared Thermography Imaging of the Plasma

As illustrated in Fig. 9 there was a significant increase in discharge optical emission intensity with the increase in discharge power. In order to evaluate how this influenced the thermal properties of the plasma, infrared thermography imaging of the plasma was performed. Thermography images obtained at low (3.7 W) and high (7.6 W) discharge powers at 5 slm

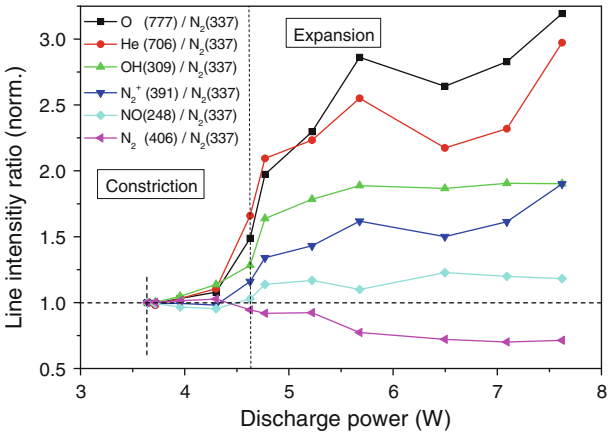

Fig. 8 Intensity ratios of different emission lines and bands at the electrode region, for a fixed helium flow rate of 5 slm and a gap distance of 2.5 mm, as a function of the discharge power. All ratios are normalized to 1 at the lowest power

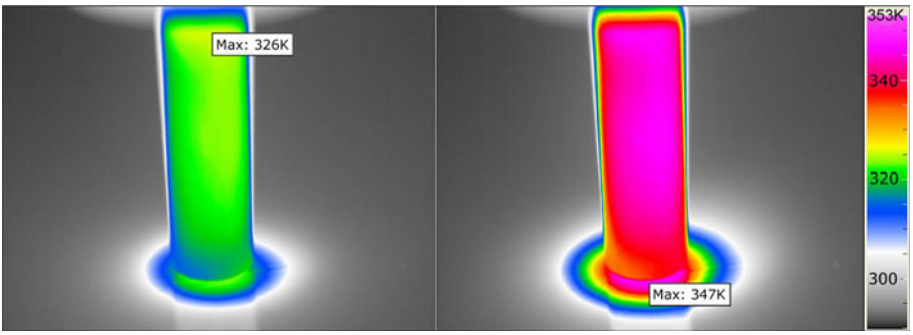

Fig. 9 Thermographic imaging at discharge power levels of 3.7 and 7.6 W. These thermal images illustrate the effect of power on the spatial temperature of the plasma discharge

helium flow are compared in Fig. 9. A local threshold algorithm was used to delineate the spatial surface temperature of the quartz tube. It can be seen at 3.7 W, that the corona discharge is localized around the electrodes where the maximum temperature 326 K is observed. However, at 7.6 W, the discharge has expanded into the quartz tube volume, and the entire tube is heated. The average quartz tube surface temperature at 3.7 W is 319 K, while at 7.6 W the quartz tube reached a temperature of 343 K. These thermal measurements agree well with wall temperature measurements reported by Herbert et al. [24].

Estimate of Heat Loss Through Gas Flow

Given the gas flow within the discharge tube is in the laminar flow regime (section"Characterization of discharge power as a function of helium flow"), Newton's law of heat transfer can be used to estimate the forced convection heat loss via helium flow see (4) and reference [21].

$$Q_H = \frac{\sigma_a}{L} NuA(\Delta T) \tag{4}$$

In (4), Q_H is the rate of heat transfer [W], σ_a is the thermal conductivity of helium gas [W/mK], L is the length of the discharge volume (nozzle) [m], Nu is the Nusselt number

$Nu = 0.664\ (Pr)^{0.3}\ (Re)^{0.5}$—the ratio of convective to conductive heat transfer; Pr is the Prandtl number (0.26 for helium); A is the area of the discharge volume [m^2], and ΔT is the change in gas temperature (difference between the maximum plasma discharge temperature and the ambient determined with thermal imaging). Therefore, for a helium gas velocity 0.4 ms^{-1}, 2.5 mm gap distance and 7.6 W discharge power, ΔT was determined as 57 K, where the ambient temperature is 290 K, and the maximum temperature of the substrate is 347 K (Fig. 9), and the forced convection heat loss is 0.07 W, which is the heat directly impacted onto the substrate.

Rotational Temperatures

The rotational temperature of the nitrogen molecules in the discharge were determined from the ($v = 0 \rightarrow 2$) emission bands of the second positive system of molecular nitrogen $N_2\left(C^3\Pi^+{}_u - B^3\Pi^+{}_g\right)$ at $\lambda = 380$ nm. The method is based on fitting a simulated spectra to the measurement points and is described in detail elsewhere [36]. It is generally considered that the population distribution among rotational sublevels of molecular nitrogen is closely coupled to the translational energy distribution of the gas. As a result, the rotational temperature is close to the kinetic gas temperature. Here, the rotational temperature T_{rot} was determined from the optical emission spectra of the persistent nitrogen gas impurities present in an open air atmospheric pressure system. The evaluation concentrates on the $\upsilon = 0 \rightarrow 2$ rotational band of the $N_2\left(C^3\Pi^+{}_u - B^3\Pi^+_g\right)$ second positive system since it has been found to be free from overlap with other spectral features and the small quantum numbers of the states means that their population distribution is likely to be closer to equilibrium The effect of increasing helium flow rates on discharge power is shown in Fig. 10. As expected, the rotational temperature was found to decrease with increasing helium flow although the discharge power increases in this range. The temperature was found to be higher at the top electrode region in comparison with the region near the nozzle exit. Overall, the rotational temperatures range from 350 to 450 K. The rotational energy distribution is usually assumed to be in equilibrium with gas molecule kinetic energy distribution and so the rotational temperature is seen to reflect the neutral gas temperature within the quartz tube [37]. These temperatures are higher than the quartz tube wall temperatures, as expected. Note that previous temperature measurements reported for this

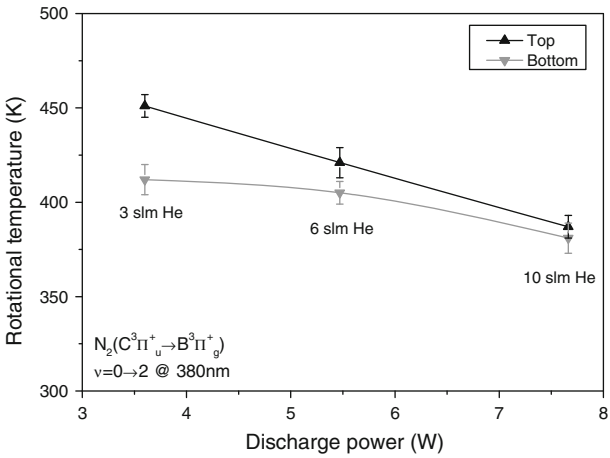

Fig. 10 The discharge power dependence of the rotational temperatures measured at the electrode region (*top*) and nozzle exit (*bottom*) and with a gap distance of 2.5 mm

plasma jet system design were not carried out in the effluent region [24]. Temperature measurements carried out in this study in the effluent region $\sim$10 mm from the nozzle resulted in a lower thermal temperature of 293 K. This indicates that the plasma activated species are rapidly cooled in the expanding effluent region to such a degree that allows heat sensitive treatment of polymeric and composite materials and many medical applications [38].

It has been shown that the temporal dependence of discharges and the presence of metastables can influence the time averaged rotational temperature of the molecules [34]. Here for example a similar analysis of the ($v = 0 \rightarrow 1$) emission band of molecular nitrogen at $\lambda = 357$ nm as well as of the ($0 \rightarrow 0$) emission band of the first negative system of molecular nitrogen ions N_2^+ ($B^2\Sigma^+_u - X^2\Sigma^+_g$) at 391 nm was performed. Similar dependencies with discharge power, helium flow and gap distance were found. However, the rotational temperatures obtained were considerably higher (up to 700 K). This may demonstrate the need for temporally resolved rotational distribution measurement to provide details on the plasma kinetics.

Conclusions

An industrial scale atmospheric pressure plasma jet system has been systematically studied by varying the helium flow from 1 to 10 slm and the gap distance from 2.5 to 7.5 mm. It was found that approximately 26% of the power developed in the high voltage line of the power supply is transferred to the discharge, where the discharge power ranged from 3.7 to 7.6 W. These discharge power calculations do not include energy loss pathways due to UV, visible and rf emission [39] for the discharge, both of which will lower the true discharge dissipated power.

From visual inspection the plasma jet operates in at least two regimes: at low powers and low helium flows (1–3 slm of helium) the discharge is constricted or localized at the electrodes where the discharge volume is increasing at a rate 1.88 cm^3/slm. When the discharge power and helium flow is increased the discharge expands into the volume of the quartz tube where it becomes more luminous. The time dependent electrical signals indicate that the constricted or localized plasma is corona/filamentary-like with chaotic temporal structure and that the volume plasma is more quiescent and glow-like occurring once each cycle of the applied voltage when the voltage is positive [34]. The computed peak current density for these discharges range from 10 to 75 mA/cm^2; this would indicate the discharge is more likely to be filamentary in the localized mode rather than corona which generally have a current density of the order of μA/cm^2.

The temperature of the plasma activated species close to the electrodes (deduced from the rotational temperature of nitrogen molecules) were found to be up to 400 $\pm$ 50 K, deceasing with helium gas flow. Thermographic imaging of the quartz tube wall indicate a lower surface temperature of 326–347 K, and heat flow calculations yield a heat transfer rate of 0.07 W to a treated surface.

From an applications perspective it was observed that the discharge operating mode changes with input power, helium gas flow and gap distance. These parameters influence the plasma kinetics and gas temperature inside the discharge, as well as the radical species flux and the spectral distribution and flux of radiation onto the treatment surface. This study provides a means of power calibration of the plasma jet and a means for estimating the heat transfer to the treatment surface. Both of which have not been reported before. These measurements allow the reported plasma processing outcome [12–19] to be

revaluated in terms of discharge power and heat transfer. Outside the nozzle the gas temperature drops towards the surface to such a degree that allows heat sensitive treatment of polymeric and composite materials and many medical applications. By selecting an appropriate gap distance of 2–3 mm and 50% of the power supply setting ($\sim$5 W discharge power), Ardhaoui et al. [16] has shown that the effective temperature and abundance of activated species can be actively engineered for cell adhesion. This conclusion also has relevance to the adhesive bonding issue highlighted in the introduction where high adhesive bond strength for siloxane elastomers bonded to coated steel were obtained at the more energetic smaller gap distances between the nozzle and the substrate.

Acknowledgments This work is supported by Science Foundation Ireland Grant 08/SRC11411 and Enterprise Ireland grant CFDTD/7/IT/304. A Nindrayog was supported by a Northern Ireland Department of Education and Learning MSc studentship. V. Milosavljevic acknowledges support by Enterprise Ireland and the Ministry of Science and Technological Development of the Republic of Serbia.

References

1. Kogelschatz U (2002) IEEE Trans Plasma Sci 30:1400–1408
2. Abolmasov S, Kroely L, Roca i Cabarrocas P (2009) Plasma Sources Sci Technol 18:015005
3. Sato M (2008) Plasma Sources Sci Technol 17:024021
4. Förster S, Mohr C, Viöl W (2005) Surf Coat Technol 200:827–830
5. Reuter S, Niemi K, Schulz-von der Gathen V, Döbele HF (2009) Plasma Sources Sci Technol 18:015006
6. Stoffels E, Flikweert A, Stoffels W, Kroesen G (2002) Plasma Sources Sci Technol 11:383–388
7. Laroussi M, Tendero C, Lu X, Alla S, Hynes WL (2006) Plasma Process Polym 3:470–473
8. Hong YC, Uhm HS (2006) Appl Phys Lett 89:221504
9. Shi JJ, Deng XT, Hall R, Punnett JD, Kong MG (2003) J Appl Phys 94:6303–6310
10. Simon A, Anghel S, Papiu M, Dinu O (2009) Nucl Instrum Methods Phys Res. B 267:438–441
11. Staack D, Farouk B, Gutsol A, Fridman A (2005) Plasma Sources Sci Technol 14:700–711
12. O'Neill L, Dobbyn P, Castagna W, Plasma system, PCT patent WO2006/048650, p 8
13. Dobbyn P, O'Neill L, Atmospheric pressure plasma, PCT patent WO2009/034012, p 25
14. Nwankire CE, Ardhaoui M, Dowling DP (2009) Polym Int 58:996–1001
15. O'Neill L, Shephard N, Leadley SR, O'Hare LA (2008) J Adhes 84:562–577
16. Ardhaoui M, Naciri M, Mullen T, Brugha C, Keenan AK, Al-Rubeai M, Dowling DP (2010) Adhes Sci Technol 24:889–903
17. Albaugh J, O'Sullivan C, O'Neill L (2008) Surf Coat Technol 203:844–847
18. O'Neill L, O'Sullivan C (2009) Chem Vap Depos 15:21–26
19. Nwankire CE, Dowling DP (2010) Adhes Sci Technol 24:1291–1302
20. www.plasmatechnics.com
21. Law VJ, Milosavljevic V, O'Connor N, Lalor JF, Daniels S (2008) Rev Sci Instrum 79:094707–094710
22. Walsh JL, Kong MG (2008) Appl Phys Lett 93:111501
23. Radu I, Bartnikas R, Wertheimer M (2003) J Phys D Appl Phys 36:1284–1291
24. Herbert PAF, O'Neill L, Jaroszynska-Wolinska J (2009) J Chem Mater 21:4401–4407
25. Dowling DP, Ramamoorthy A, Rahman M, Mooney DA, MacElroy JMD (2009) Plasma Process Polym 6:S483–S489
26. Chang J, Lawless P, Yamamoto T (1991) IEEE Trans Plasma Sci 19:1152–1166
27. Law VJ, O'Connor N, Daniels S (2008) Piers Online 4:556–560
28. Law VJ (2008) Vacuum 82:630–638
29. Jidenko N, Petit M, Borra JP (2006) J Phys D Appl Phys 39:281–293
30. Sun W, Liang T, Wang H, Li H, Bao C (2007) Plasma Sources Sci Technol 16:290–296
31. Law VJ, O'Connor N, Twomey B, Dowling DP, Daniels S (2009) In: Skiadas CH et al (eds) Topics of chaotic systems: selected papers of chaos 2008 international conference. World scientific publishing, pp 204–213, 978–981-4271-33-2
32. Benedikt J, Focke K, Yanguas-Gil A, von Keudell A (2006) Appl Phys Lett 89:251504
33. Pouvesle JM, Bouchoule A, Stevefelt J (1982) J Chem Phys 77:817–825
34. Nersisyan G, Graham WG (2004) Plasma Sources Sci Technol 13:582–587

35. Bibinov NK, Fateev AA, Wiesemann K (2001) J Phys D Appl Phys 34:1819–1826
36. Twomey B, Nindrayog A, Niemi K, Graham WG, Dowling DP (2010) Plasma Chem Plasma Process PCPP-10-SV-0006 (submitted)
37. Laux C, Spence T, Kruger C, Zare R (2003) Plasma Sources Sci Technol 12:125–138
38. Kong MG, Kroesen G, Morfill G, Nosenko T, Shimizu T, Dijk Jv, Zimmermann JL (2009) New J Phys 11:115012
39. Law VJ, Daniels S, Walsh JL, Kong MG, Graham LM, Gans T (2010) Plasma Sources Sci Technol 19:034008